

Antivesiculation and Complete Unbinding of Tail-Tethered Lipids

K. Shih, L. Yang

To be published in "Langmuir"

February 2024

Photon Sciences

Brookhaven National Laboratory

U.S. Department of Energy

USDOE Office of Science (SC), Basic Energy Sciences (BES). Scientific User Facilities (SUF)

Notice: This manuscript has been authored by employees of Brookhaven Science Associates, LLC under Contract No. DE-SC0012704 with the U.S. Department of Energy. The publisher by accepting the manuscript for publication acknowledges that the United States Government retains a non-exclusive, paid-up, irrevocable, world-wide license to publish or reproduce the published form of this manuscript, or allow others to do so, for United States Government purposes.

DISCLAIMER

This report was prepared as an account of work sponsored by an agency of the United States Government. Neither the United States Government nor any agency thereof, nor any of their employees, nor any of their contractors, subcontractors, or their employees, makes any warranty, express or implied, or assumes any legal liability or responsibility for the accuracy, completeness, or any third party's use or the results of such use of any information, apparatus, product, or process disclosed, or represents that its use would not infringe privately owned rights. Reference herein to any specific commercial product, process, or service by trade name, trademark, manufacturer, or otherwise, does not necessarily constitute or imply its endorsement, recommendation, or favoring by the United States Government or any agency thereof or its contractors or subcontractors. The views and opinions of authors expressed herein do not necessarily state or reflect those of the United States Government or any agency thereof.

Anti-Vesiculation and Complete Unbinding of Tail-Tethered Lipids

Kuo-Chih Shih¹, Geoffray Leriche², Chung-Hao Liu¹, Jibao He³, Vijay T. John³, Justin Fang⁴, John G. Barker⁵, Michihiro Nagao^{5,6,7}, Lin Yang⁸, Jerry Yang² & Mu-Ping Nieh^{*1,4,9}

¹Polymer Program, Institute of Materials Science, ⁴Department of Biomedical Engineering, ⁹Department of Chemical and Biomolecular Engineering, University of Connecticut, Storrs, CT 06269, USA

²Department of Chemistry and Biochemistry, University of California, San Diego, La Jolla, CA 92093, USA

³Department of Chemical and Biomolecular Engineering, Tulane University, New Orleans, LA 70118, USA

⁵NIST Center for Neutron Research, National Institute of Standards and Technology, Gaithersburg, MD 20899, USA

⁶Department of Materials Science and Engineering, University of Maryland, College Park, MD 20742, USA

⁷Department of Physics and Astronomy, University of Delaware, Newark, DE 19716, USA

⁸National Synchrotron Light Source II, Brookhaven National Laboratory, Upton, NY 11973, USA

* Corresponding authors. Tel.: +1 8604868708 E-mail addresses: mu-ping.nieh@uconn.edu

Abstract

We report the effect of tail-tethering on vesiculation and complete unbinding of bilayered membranes. Amphiphilic molecules of a bolalipid, resembling the tail-tethered molecular structure of archaeal lipids, with two identical zwitterionic phosphatidylcholine headgroups self-assembles into large flat lamellar membrane, in contrast to the multilamellar vesicles (MLVs) observed in its counterpart, mono-polar non-tethered zwitterionic lipids. The anti-vesiculation is confirmed by small angle X-ray scattering and cryogenic transmission electron microscopy. With the net charge of zero and higher bending rigidity of the membrane (confirmed by neutron spin echo spectroscopy), the current membrane theory would predict that membranes should stack with each other (aka “bind”) due to dominant van der Waals attraction, while the outcome of non-stacking (“unbinding”) membrane suggests that the theory needs to include entropic contribution for the non-vesicular structures. This report pioneers in understanding how the tail-tethering of amphiphiles affects structure, enabling better control over the final nanoscale morphology.

Introduction

Biological membranes play important roles in performing crucial biological functions more than defining the boundary of cells, organelles, bacteria, *etc.* They also control the transport of materials across the membranes with the help of membrane proteins. As phospholipids are the building blocks of biological membranes, during the last two decades studies have been focusing on probing the properties of phospholipid bilayer such as membrane stiffness¹⁻⁷, inter-leaflet coupling⁸⁻¹² domain formation/phase separation¹³⁻¹⁷ and perforation¹⁸⁻²¹. Most of phospholipids have a hydrophilic polar (monopolar) headgroup and one or more hydrophobic hydrocarbon tails. A unique type of them found in the archaeal membrane named bipolar lipids, also known as “bolalipids”, have a molecular structure resembling two identical lipids with one or more tails covalently tethered²². The chemical tethering leads to the formation of monolayer, instead of bilayer, membranes. The fact that some archaea with such bolalipid membrane can survive high temperatures and highly acidic environments is partially attributed to the extraordinary stability of the membrane and has drawn a great deal of research attentions²³⁻²⁶. High viscosity²⁷ and low permeability^{28,29} have been experimentally observed in bolalipids. Presumptions of and molecular simulations on high membrane rigidity also suggest the importance of the tail-tethering^{27,28,30}. Although the tail-tethering is fundamentally important and expectedly pertaining to the unique properties of archaea, systematic experimental approaches have not been taken partially because of the low yield (at the level of milligrams) from the complex extraction and purification process of natural archaeal lipids³¹. Such information can affect the rational design for stable membrane structure. Recently, a large-scale synthetic strategy for preparing bipolar tethered lipids (on the order of grams)^{30,32,33} has been developed, enabling us to investigate the system further to provide insight into how tail-tethering affects the system.

Lipid bilayers made of monopolar lipids with a molecular critical packing parameter between 0.5 and 1 tends to form vesicles. The energy penalty of the hydrophobic tails being exposed to the aqueous environment can be minimized by forming multilamellar vesicle (MLV) or unilamellar vesicle (ULV). Theoretically, the lamellarity is dictated by the minimal energy of the system. Eq (1) summarizes the possible contributions of energy to a bilayer membrane system, including the electrostatic (Coulombic) energy between two membranes, $V_E(D)$, the hydration energy, $V_H(D)$ the van der Waals attraction energy, $V_{vdw}(D)$, and the steric hindrance of the two adjacent bilayer membranes due to thermal undulation, $V_S(D)$ ³⁴, where D is the inter-lamellar d -spacing of the bilayer membranes. Note that the value of $V(D)$ will be at the order of $-10^{-26} \frac{J}{nm^2}$ to $-10^{-24} \frac{J}{nm^2}$

$$V(D) = V_E(D) + V_H(D) + V_{vdw}(D) + V_S(D) \quad (1)$$

MLVs present the equilibrium outcome from an overwhelming attractive $V_{vdw}(D)$ compared to the repulsive $V_S(D)$, $V_E(D)$ and $V_H(D)$. This theory successfully explains the MLV with a well-defined D observed in most of the zwitterionic phospholipid bilayers, while MLVs can undergo an “unbinding” transition to form ULVs when charged lipids are introduced to the system where $V_E(D) + V_S(D)$ overwhelms $V_{vdw}(D)$. Experimental evidence also confirmed that thermal energy could trigger a reversible MLV-to-ULV transition of a bilayer membrane after a careful manipulation of the charge density of lipids and the salinity of solution to balance the effects of $V_{vdw}(D)$ and $V_E(D)$.^{35,36} Another study also reported that the interplay of the $V_E(D)$ and $V_S(D)$ can induce the membrane unbinding³⁷. Moreover, a recent report has shown that introduction of charged lipid can induce 90 % of ULV in a zwitterionic lipid MLV solution.³⁸ Another report shows that reversible transition of MLV-to-ULV in a cationic liposomal system through thermal energy.³⁹ Since thermal undulation induced $V_S(D)$ can be dampened by membrane rigidity, *more rigid membranes expectedly yield lower $V_S(D)$, thus promoting the formation of MLVs*. The

membrane rigidity can be revealed from the decay rate of the scattering intensity at a specific scattering vector, q through a neutron spin echo scattering (NSE) experiment. Detailed explanation on application of NSE to probing membrane dynamics and membrane rigidity can be found in the literatures.⁴⁰⁻⁴²

Here, we report an unexpected complete “unbinding” of a bipolar tethered zwitterionic lipid membrane (glycerol hexadecane glycerol tetraether lipids with 32 carbon tethered chain and phosphocholine headgroups, GHGTPC-T32) with a chemical structure shown in Fig. 1 (a). The self-assembly of GHGTPC-T32 forms large lamellae in contrast to the MLVs observed in its monopolar non-tethered counterpart, 1,2-di-O-hexadecyl-*sn*-glycero-3-phosphocholine [DC_{16:0}etherPC, Fig 1(b)] in aqueous solutions. We have also shown that Eq (1) is inadequate to fully describe the lamellarity of tail-tethered lipid (GHGTPC-T32) because of the missing term for entropic contribution. For this reason, Eq (1) would need to be corrected by additional entropic energy.

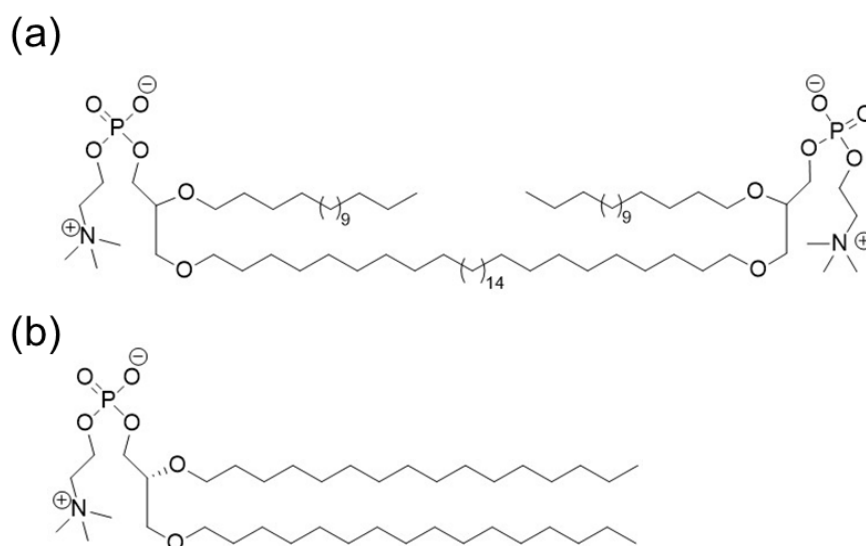


Figure 1. Chemical structures of (a) bolalipid, GHGTPC-T32 and (b) monopolar lipid DC_{16:0}etherPC.

Results and Discussions

Self-Assemble Structure of GHGTPC-T32

Fig 2(a) shows two distinct small-angle X-ray scattering (SAXS) patterns as a function of scattering vector, q from the GHGTPC-T32 and DC_{16:0}etherPC aqueous solutions at 25 °C. It should be noted that the samples self-assembled without sonication or extrusion. The scattering data of GHGTPC-T32 follows a q^{-2} decay in the low q regime ($< 0.02 \text{ \AA}^{-1}$), suggesting a layered structure with lateral dimensions larger than 100 nm. The SAXS data of its counterpart, DC_{16:0}etherPC, on the contrary exhibit three orders of sharp Bragg peaks (q_1 , q_2 and q_3 being 0.13 \AA^{-1} , 0.26 \AA^{-1} and 0.39 \AA^{-1}) corresponding to an MLV structure, revealing an interlamellar spacing, $D (= \frac{2\pi}{q_1})$ of 48.3 \AA . MLV is a common morphology of zwitterionic phospholipid yielding the lowest energy. The measured value of D is significantly lower than those from many other MLVs made of phospholipid with similar chain lengths (between 60 \AA and 70 \AA when fully hydrated^{43,44}, but consistent with a previously reported value for DC_{16:0}etherPC membrane because of an interdigitated gel phase ($L_{\beta I}$)⁴⁵. On contrary, no such sharp Bragg reflections are found in the SAXS data of the tail-tethered GHGTPC-T32 solution, suggesting the absence of GHGTPC-T32 MLVs. Apparently, tail-tethering results in a drastic effect on the final morphology. Cryogenic transmission electron micrographs (cryo-TEM) of GHGPC-T32 and DC_{16:0}etherPC [Figure 3(a) and 3(b)] demonstrate large lamellae (with sharp, straight-line edges indicated by the blue arrow) and MLVs, respectively, agreeing to the negatively stained TEM image in previous report on a similar system^{46,47}. Since both SAXS data and cryo-TEM results suggest no long-range stacking of GHGTPC-T32 membrane, this demands an explanation for the cause of anomalous anti-vesiculation phenomenon. We further analyze the SAXS patterns to reveal the internal structure of the GHGTPC-T32 membrane.

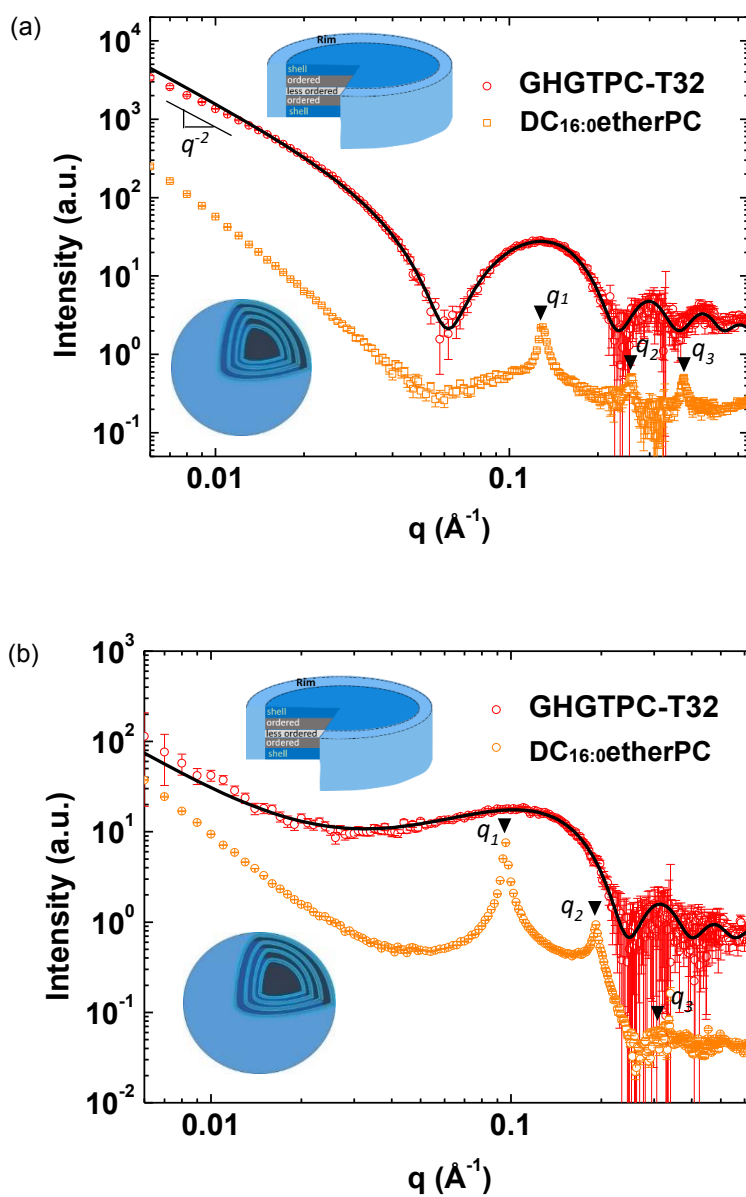


Figure 2. SAXS patterns for 1 % GHGTPC-T32 (red) and DC_{16:0}etherPC (orange) measured at (a) 25 °C and (b) 72 °C. The solid curves are best fits to the data of GHGTPC-T32 using 5LCSD model. Error bars represent one standard deviation throughout the manuscript and are smaller than the data symbols in some cases.

The SAXS profile of GHGTPC-T32 can be described as a 5-layer core-shell disc (5LCSD) model (detailed description of this model is provided in the Supporting Information)⁴⁸, where the electron scattering length density (eSLD) profile across the membrane is described by five distinct layers

(phosphate – ordered hydrocarbon – less ordered hydrocarbon – ordered hydrocarbon – phosphate). The best-fitting monolayer thickness of $\approx (46.5 \pm 5.6)$ Å with the headgroup size and hydrophobic tail of $\approx (5.6 \pm 1.0)$ Å and $\approx (35.3 \pm 3.6)$ Å (tethered chain length), respectively (Table 1), close to the reported DC_{16:0}etherPC headgroup peak-peak distance ($D_{HH} = 45.6$ Å)⁴⁵, implying high similarity of the thickness of these two lipid bi-/mono- layer. The minimal attainable q , q_{min} (≈ 0.006 Å⁻¹) of the current SAXS configuration limits the best fit to determine the lateral dimension of the membrane fragment, which is at least larger than $\approx 1,000$ Å ($2\pi/q_{min}$).

Table 1. The best fitting parameters of the GHGTPC-T32 samples at 25 °C and 72 °C based on SAXS data (The fitting uncertainty listed is ± 1 standard deviation)

	25°C	72°C
core radius (Å)	>1000	>1000
rim (Å)	28.8 ± 1.5	40.0 ± 0.03
phosphate shell thickness(Å)	5.6 ± 1.0	5.6 ± 1.1
ordered hydrocarbon thickness (Å)	12.8 ± 1.2	8.5 ± 1.0
less-ordered hydrocarbon thickness (Å)	9.7 ± 1.2	16.2 ± 1.2
eSLD, ordered ($\times 10^{-6}$ Å ²)	9.38 ± 0.02	9.20 ± 0.11
eSLD, less-ordered ($\times 10^{-6}$ Å ²)	9.09 ± 0.06	8.80 ± 0.13
eSLD, shell ($\times 10^{-6}$ Å ²)	11.1 ± 0.04	10.7 ± 0.14
eSLD, rim ($\times 10^{-6}$ Å ²)	9.54 ± 0.02	9.60 ± 0.10
eSLD_Solvent ($\times 10^{-6}$ Å ²)	9.47 (Fixed)	9.47 (Fixed)
background (cm ⁻¹)	0.1 (Fixed)	0.06 (Fixed)

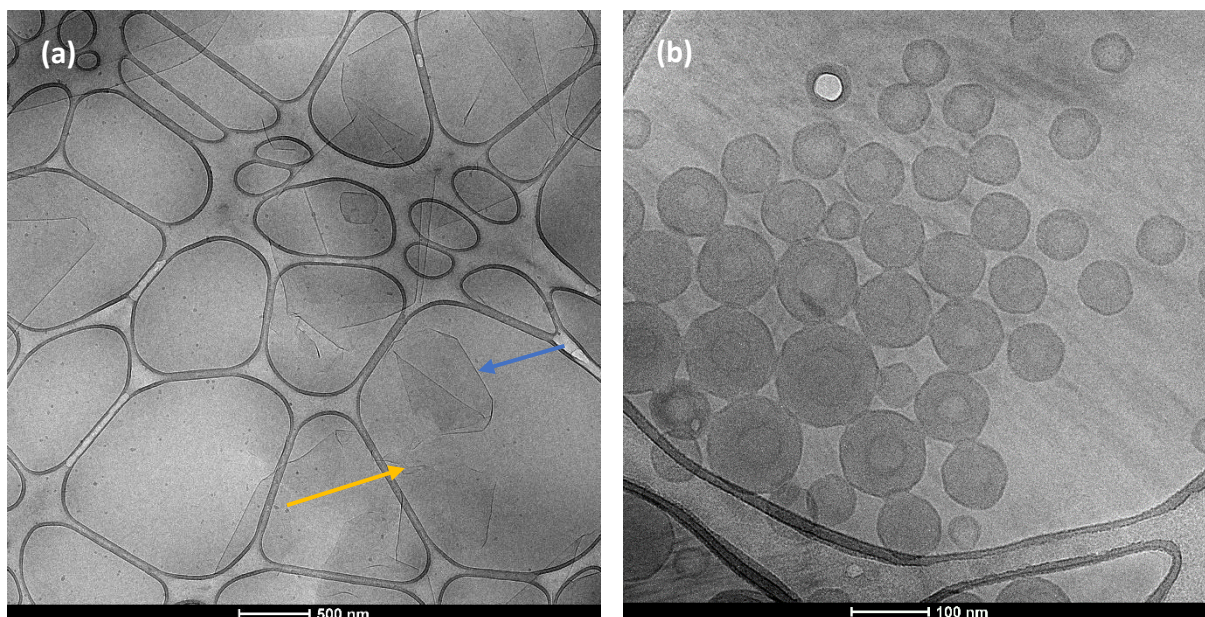


Figure 3. Cryo-TEM micrographs of (a) GHGTPC-T32 large extended lamellar sheets and (b) DC_{16:0}etherPC MLVs. The orange and blue arrows [in (a)] point at the crumpled edge and regular edge of the lamellar sheet, respectively.

Anti-vesiculation of the GHGTPC-T32

Geometrically, the exterior water-lipid interface of a vesicle is always larger than the interior one. For non-tethered monopolar lipids like DC_{16:0}etherPC, it is therefore expected that more lipid molecules are located at outer than inner leaflet of a bilayer. For tethered GHGTPC-T32, the number of polar headgroups is expected to be identical on either side of the membrane at its minimal energy. To undergo vesiculation, either uneven numbers of headgroups at the outer and inner leaflets or the “splay” of lipid molecules around the vesicular center has to take place. Both would lead to high energy penalty.⁴⁹ The former case requires the tethered tails to adopt a U-shape (hairpin) configuration, resulting in high energy penalty.⁵⁰ ²H NMR and MD simulation studied on GHGTPC-T20,⁵¹ tethered DMPC (1,2-dimyristoyl-sn-glycero-3-phosphocholine)⁵² and tethered DPPC (1,2-dimyristoyl-sn-glycero-3-phosphocholine),⁵³ suggest little or no U-shape configuration [Fig 4 (a)] would exist in the system. The latter case would increase the energy

penalty due to enhanced water-hydrocarbon interface and destruction of the crystallinity of hydrocarbon chains.

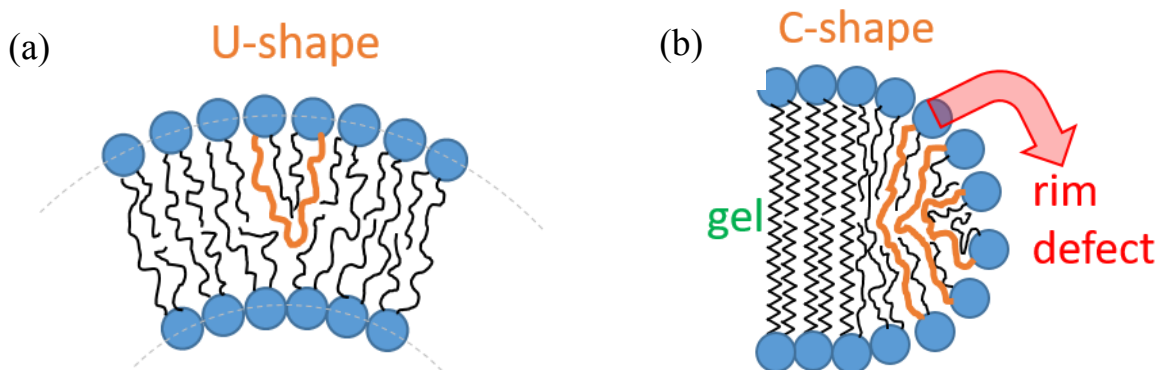


Figure 4. (a) The schematic of a “U-shape” (orange) tethered tail required for vesiculation – yielding uneven numbers of headgroup in outer and inner leaflets. (b) The edge of bilipid membrane fragment stabilized by the “rim defect”, where lipids may adopt non-crystalline fluidic phase in contrast to the crystalline gel phase in the planar region. The “orange” tethered-tails demonstrate the proposed “C-shape” configurations.

We attempted to provide the insight into the energy cost of the U-shape configuration via high- T SAXS data ($T = 72\text{ }^{\circ}\text{C} > T_m$ where T_m is the melting temperature of the lipid) of GHGTPC-T32 and DC_{16:0}etherPC [Fig 2(b)]. Theoretically more U-shape configuration could be adopted at 72 °C, enabling vesiculation for two reasons. First, the thermal energy would favor the formation of high-energy U-shape configuration. Second, the melted hydrophobic tails would reduce the energy penalty for the U-shape configuration. As a result, the same 5LCSD model can fit the high- T SAXS data of GHGTPC-T32 even though the scattering pattern is different from that at 25 °C. The fact that no evidence for vesiculation and no Bragg reflections of MLVs are observed indirectly negates the U-configuration at low T . Instead, the best fitting parameters (Table 1) only show a thicker middle “less-ordered” hydrophobic regime and increased rim thickness, implicative of loosely

packed hydrocarbon chains. The rim of GHGTPC-T32 fragment is hypothetically stabilized by lipids with a “C-shape” configuration *with a smaller bending angle* [Fig 4(b)] than U-shape configuration, where both phosphate groups are forced to be on the same side of the membrane [Fig 4(a)]. Such C-shape configuration prevents the exposure of hydrophobic chains to water. As a result, the formation of membrane fragment requires less energy than vesiculation, which demands U-shape configuration of GHGTPC-T32 to yield more phosphate groups at the outer leaflet than that at the inner one. In contrast, the high- T SAXS data of the monopolar lipid DC_{16:0}etherPC suggest MLV structure with an increased D -spacing (65 Å), presumably attributed to the combined effect of enhanced $V_S(D)$ with elevated thermal undulation [see Eq(1)] and decoupling of interdigitated leaflets (hence a thicker bilayer).

Non-stacking of the GHGTPC-T32

It is reasonable to assume that the van der Waals attraction [$V_{vdw}(D)$], Coulombic repulsion [$V_E(D)$] and hydration interaction [$V_H(D)$] in Eq (1) are identical for GHGTPC-T32 and DC_{16:0}etherPC since these two lipids have the identical hydrophilic headgroup and similar hydrophobic molecular architectures except for the tethering of the end carbons. This leaves V_S , associated with the steric repulsion, the only term subjected to change in Eq (1). To inhibit the stacking of GHGTPC-T32 membranes, strong steric repulsion (V_S) is required. In other words, GHGTPC-T32 has to be less rigid than DC_{16:0}etherPC. Nevertheless, tethered lipid is expected to be more rigid than its non-tethered counterpart because of the reduced mobility,²⁸ consequently leading to reduced intermembrane steric repulsion. The higher melting transition temperature, T_m , of GHGTPC-T32 (67 °C) obtained from differential scanning calorimetry (Fig. S1) than that of DC_{16:0}etherPC (44 °C) also agrees with the anticipated less mobility of the GHGTPC-T32

membrane. The unexpected “unbinding” of GHGTPC-T32 membrane intrigues our interest in the bending moduli of the two lipid membranes.

Direct measurement of the effective bending modulus, κ_{eff} , of membrane can be achieved by neutron spin echo (NSE) spectroscopy. Fig 5 (a) and (b) illustrate the normalized intermediate scattering function, $\frac{I(q,t)}{I(q,0)}$, versus Fourier time, t , for GHGTPC-T32 and DC_{16:0}etherPC, respectively. Since the lamellarity affects the interaction between lipid bilayers, NSE samples are measured with extrusion only for the DC_{16:0}etherPC sample. SAXS result indicates that MLV does not form in the GHGTPC-T32 sample. The intensity decay of NSE result follows a stretched exponential function, $\frac{I(q,t)}{I(q,0)} \cong \exp[-(\Gamma_{ZG}t)^{2/3}]$, where Γ_{ZG} is the decay rate as proposed by Zilman and Granek for membrane bending fluctuations based on Helfrich’s model that treats the membrane as a thin elastic sheet.^{54,55} The GHGTPC-T32 membrane fragments are sufficiently large to satisfy Zilman and Granek’s framework in the measured space and time scales for NSE experiments.

We fit the intermediate scattering function by using $\frac{I(q,t)}{I(q,0)} \cong \exp[-(\Gamma_{ZG}t)^{2/3}] \times \exp(-D_T q^2 t)$,⁵⁶ where D is the translational diffusion coefficient of the particle. The term, $\exp(-D_T q^2 t)$ accounts for the different hydrodynamic radii, R_H of GHGTPC-T32 and DC_{16:0}etherPC (≈ 600 nm and ≈ 50 nm, respectively, from dynamic light scattering, Fig. S2). From the Stokes-Einstein equation, D_T can be expressed as $k_B T / 6\pi\eta R_H$, where k_B , T , and η are Boltzmann constant, absolute temperature and solvent viscosity, respectively. It should be noted that the large R_H of GHGTPC-T32 negates the vesicular morphology as the highest achievable lipid concentration (at the highest packing density) should be less than 2% for vesicles with a

radius of 600 nm and a bilayer thickness of 5 nm, a consistent observation with the cryo-TEM and SAXS outcome.

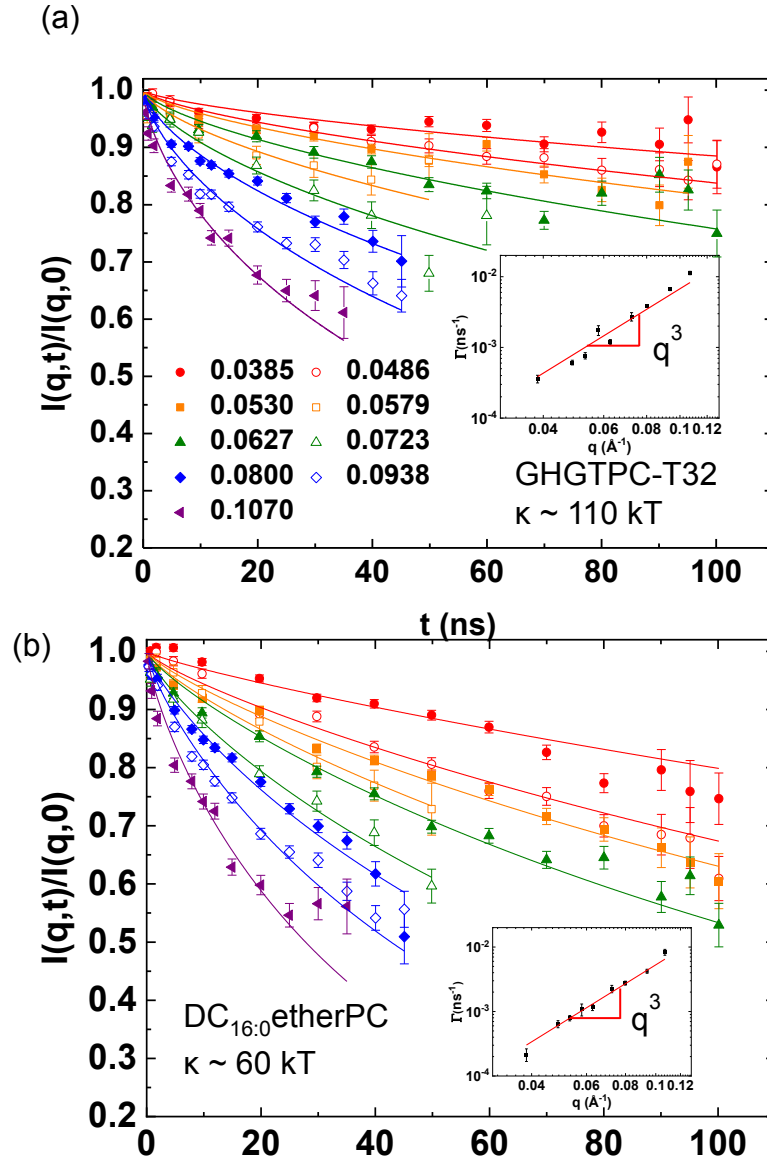


Figure 5. Normalized intermediate scattering function, $\frac{I(q,t)}{I(q,0)}$, measured by NSE at 72 °C. (a) GHGTPC-T32 and (b) DC_{16:0}etherPC. The inset in each figure shows the linear dependence of Γ_{ZG} and q^3 . Note that the q values chosen in both graphs are the same.

Γ_{ZG} is linearly scaled with q^3 as shown in the inset of Fig. 5 (a) and (b). Then, the bending modulus can be extracted including Watson and Brown's refinement⁵⁷ by using the following Eq (2).⁵

$$\frac{\Gamma_{ZG}}{q^3} = 0.0069 \sqrt{\frac{k_B T}{\kappa_{eff}} \frac{k_B T}{\eta}} \quad (2)$$

The bending modulus, κ_{eff} was found to be $\approx 110 k_B T$ and $60 k_B T$ for the GHGTPC-T32 and DC_{16:0}etherPC lipids, respectively. If diffusion of the particles were not to be considered as reported in literature,⁵⁸⁻⁶⁰ the difference in κ_{eff} would be even more significant (i.e., $\approx 90 k_B T$ for GHGTPC-T32 and $\approx 25 k_B T$ for DC_{16:0}etherPC). These results confirm the anticipated higher bending rigidity of the tethered GHGTPC-T32 than that of its counterpart, DC_{16:0}etherPC. Moreover, κ_{eff} is expected to be even higher at room T than high T (i.e., 72°C), leading to lower steric repulsion. The higher bending modulus of GHGTPC-T32 obtained from NSE agrees with all previous reports on bipolar tethered lipids^{27,61-63}. Molecular tethering of lipids plays a role in regulating flexibility and fluidity of archaeal membranes at elevated temperatures to maintain the membrane integrity. Here, for the first time, we reveal the relationship between the membrane rigidity and molecular tethering of lipid tail by NSE.

Since higher bending rigidity of GHGTPC-T32 is found, a lower $V_S(D)$ in comparison with that of DC_{16:0}etherPC. According to Eq. (1) we would expect that stronger coupling between membranes should be observed in GHGTPC-T32 considering a similar $V_{vdw}(D)$ of the two lipids. We raise a consequential question, “Why do **not** GHGTPC-T32 membranes form ‘lamellar stacks’ like DC_{16:0}etherPC MLVs as predicted by Eq (1)?”. It is noteworthy that Eq. (1) mainly considers the *energetic* interactions but ignores the *entropic* contribution of water. Moreover, the entropy of entrapped water in MLVs is significantly lower than that of free water. A molecular dynamic simulation suggests that the entropy of water between bilayer stacking decreases $\sim 16\%$ from that of free bulk water.⁶⁴ We assign the D -spacing of the DC_{16:0}etherPC MLVs (6.5 nm) for GHGTPC-T32 in the following calculation as if they would stack like DC_{16:0}etherPC. For a membrane with a thickness, $D_{lip} = 4.4 \sim 4.7$ nm (from Table 1, $D_{lip} = 2 \times$ shell thickness + $2 \times$ ordered hydrocarbon

+ disordered hydrocarbon) the derived thickness of water layer sandwiched between two membranes, D_w would be 2.1 ~ 1.9 nm. Based on the assumption of perfect 2-D object (i.e., lamellae without defects), the volume ratio of sandwiched water to lipid should be $\frac{D_w}{D_{lip}}$ (between 0.4 and 0.47). If the volume fraction of lipid is ϕ , (e.g., 0.05 in the SAXS experiment), the volume ratio of lipid to total water can be deduced to be $\frac{\phi}{1-\phi}$. The volume fraction of sandwiched water to total water can therefore be calculated as $\frac{D_w}{D_{lip}} \frac{\phi}{1-\phi}$. The reduced entropy of “less mobile” water due to membrane stacking, ΔS_{stack} can be hence estimated:

$$\Delta S_{stack} = -k_B \left[-\frac{D_w}{D_{lip}} \frac{\phi}{1-\phi} \ln \left(\frac{D_w}{D_{lip}} \frac{\phi}{1-\phi} \right) \right] \cdot 16\% \approx -0.013 k_B \sim -0.0146 k_B, \quad (2)$$

Eq. (2) results in an increased free energy of $-T\Delta S_{stack} \approx 5.4 \sim 6.1 \times 10^{-23} J$ per molecule if membranes would stack. It is reported that the calculated energy gain from van der Waal attraction, V_{vdw} ($D = 6.5$ nm) between two membranes with a thickness of 5 nm (similar to the bilayer thickness in our case) is in the range of $-10^{-23} \frac{J}{nm^2}$ to $-10^{-24} \frac{J}{nm^2}$.³⁴ Since the molecular area of a lipid, A_{lip} has been estimated in between 0.6 nm^2 to 0.65 nm^2 ,^{44,65} we estimate the energy change due to the attraction force induced by membrane stacking, $\Delta H_{stack} \sim (-10^{-23} \frac{J}{nm^2}$ to $-10^{-24} \frac{J}{nm^2}) \chi A_{lip}$, yielding $-6 \times 10^{-24} J$ to $-6 \times 10^{-25} J$ per molecule in the mixture, which is at least an order of magnitude lower than the energy penalty from the reduced entropy due to membrane stacking. The estimate does not even take the thermal fluctuation (related to V_s) into account which further counteracts V_{vdw} . Hence, the free energy of stacking membranes, $\Delta G_{stack} [\equiv \Delta H_{stack} - T\Delta S_{stack}]$ is always positive, indicating that stacking configuration is not favorable for the membrane fragments. Note that *in the case of vesicle* (instead of extended lamellae), MLVs can release more free water molecules (not being enclosed in the compartment) than non-stacking

unilamellar vesicles, yielding higher entropy, consequently reducing the Gibbs free energy through stacking, justifying why DC_{16:0}etherPC lipids form MLVs.

Conclusions

We have discovered the unique effect of tail-tethering of a bolalipid, GHGTPC-T32, on the anti-vesiculation due to the high energy penalty caused by the U-shape (hairpin) configuration of the tethered chain as vesiculation requires unequal numbers of polar headgroups between the outer and inner membrane leaflets. As a result, GHGTPC-T32 forms large lamellar sheets instead of the MLVs found in the solution of its monopolar headgroup counterpart, DC_{16:0}etherPC. Moreover, the GHGTPC-T32 lamellae do not stack despite higher rigidity than the vesicular DC_{16:0}etherPC. This “unbinding” phenomenon cannot be explained by the established traditional membrane theory because the entropic loss from the “less mobile” water sandwiched between the membranes outweighs the energy gain from the van der Waal attraction. This report provides the fundamental understanding of how molecular architecture and water dynamics can affect the morphology of a membrane system. The knowledge provides another parameter tailor the design of self-assemblies in addition to hydrophobic interaction, spontaneous curvature, and segregation between ordered and disordered phases. The anti-vesiculation due to tail-tethering is expectedly dependent on the length of tethered hydrocarbon chain because the energy of U-configuration (hairpin) should be lower with a longer chain. The future work aims to focus on determination on the critical chain length of the tethered lipids for vesiculation.

Experimental Section

1. General Materials

List of abbreviations: Ethyl acetate (EtOAc), Methanol (MeOH), Tetrahydrofuran (THF), Sodium sulfate (Na_2SO_4), Dichloromethane (DCM), Hydrochloric acid (HCl), Ethanol (EtOH), Palladium hydroxide ($\text{Pd}(\text{OH})_2$), Dimethylsulfoxide (DMSO), Acetonitrile (ACN).

All reagents were purchased from commercial sources and used without further purification. Glassware was dried at 115 °C overnight. Air and moisture-sensitive reagents were transferred using a syringe or stainless-steel cannula. Intermediates were purified over silica (60 Å, particle size 40 µm to 63 µm, Dynamic Adsorbents, Inc). Reactions were monitored by thin-layer chromatography (TLC) using 0.25 mm silica gel plates (60F-254, Dynamic Adsorbents, Inc). Deuterated solvents were purchased from Cambridge Isotope Laboratories, Inc. ^1H , ^{13}C , ^{31}P NMR spectra were recorded on either JEOL ECA 500 spectrometer or Varian 500 MHz spectrometer. Chemical shifts are reported in ppm relative to residual solvent. The FID file was analyzed using Mnova-Mestrelab.

2. Synthesis of GHGTPC-T32 bolalipid

The synthesis of GHGTPC-T32 follows the strategy in Figure 6 and the NMR spectrums are shown in the supporting information (Figure S4 -S6).

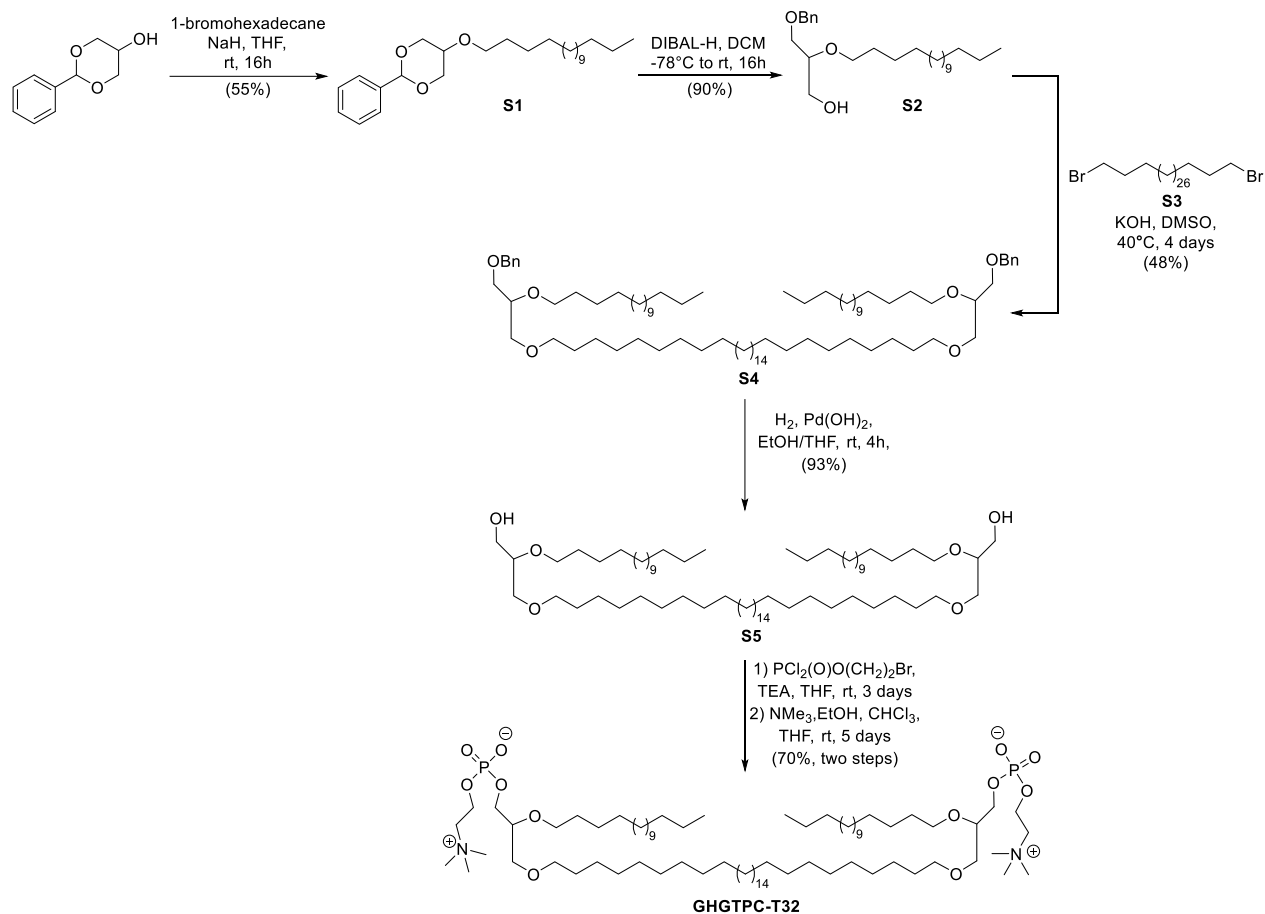
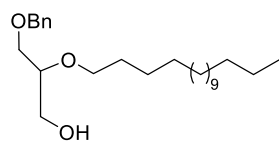


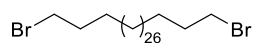
Figure 6 Synthetic scheme for **GHGTPC-T32**

3-(benzyloxy)-2-(hexadecyloxy)propan-1-ol (S2)



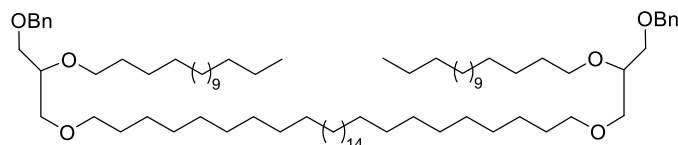
Compound **S2** was synthesized following a reported protocol.⁶⁶

1,32-dibromodotriacontane (S3)



Compound **S3** was synthesized following a reported protocol.⁶⁷

18,55-bis((benzyloxy)methyl)-17,20,53,56-tetraoxadoheptacontane (S4)



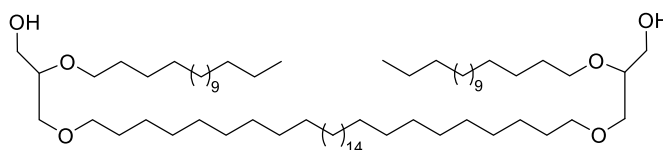
A suspension of KOH (0.71 g, 12.7 mmol) in dry DMSO (20 mL) was stirred at room temperature for 30 minutes. The mixture

was cooled with ice water and a solution of **S2** (1.95 g, 4.80 mmol) and **S3** (0.65 g, 1.07 mmol) in

dry DMSO (5 mL) was added. The mixture was then stirred at room temperature for 16 hours and then at 40 °C for 3 days. Water (300 mL) was added and the mixture was extracted with EtOAc (5x50 mL). The combined organic layers were washed with water (2x100 mL), brine (100 mL) and dried over Na₂SO₄. Purification by silica gel column chromatography using hexane/EtOAc (95:5) as the eluent yielded **S4** (0.64 g, 48 %) as a white solid.

¹H NMR (500 MHz, CDCl₃-d₁) δ 7.38 – 7.25 (m, 10H), 4.57 (s, 4H), 3.68 – 3.41 (m, 18H), 1.64 – 1.52 (m, 8H), 1.44 – 1.15 (m, 108H), 0.90 (t, *J* = 6.8 Hz, 6H); ¹³C NMR (126 MHz, CDCl₃-d₁) δ 138.6, 128.4, 127.7, 127.6, 78.1, 77.5, 77.2, 77.0, 73.5, 71.8, 70.9, 70.7, 70.4, 32.1, 30.3, 29.9, 29.8, 29.6, 29.5, 26.3, 26.3, 22.9, 14.3. (Figure S4)

2-(hexadecyloxy)-3-((32-(2-(hexadecyloxy)-3-hydroxypropoxy)dotriacontyl)oxy)propan-1-ol
(**S5**)

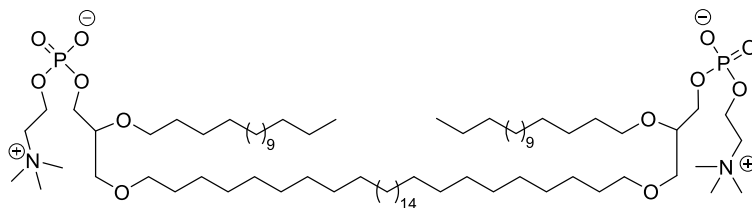


Compound **S4** (640 mg, 0.51 mmol) was dissolved in a degassed mixture of EtOH/THF (1:1, 40 mL) and 20 % Pd(OH)₂

(55 mg, 10 % w/w) was added. The reaction was stirred under hydrogen atmosphere at room temperature for 4 hours. The catalyst was removed by filtration through a pad of celite, and the resulting residue was purified by column chromatography on silica gel using CHCl₃/EtOAc (9:1 to 7:3) as the eluent. Diol **S5** (510 mg, 93 %) was obtained as a white solid.

¹H NMR (500 MHz, CDCl₃-d₁) δ 3.75 – 3.41 (m, 20H), 1.56 (q, *J* = 7.0 Hz, 8H), 1.25 (d, *J* = 1.4 Hz, 108H), 0.91 – 0.83 (m, 6H); ¹³C NMR (126 MHz, CDCl₃-d₁) δ 78.5, 77.6, 77.3, 77.0, 72.1, 71.1, 70.6, 63.3, 32.2, 30.3, 30.0, 29.9, 29.9, 29.9, 29.9, 29.7, 29.6, 26.3, 22.9, 14.4. (Figure S5)

(dotriacontane-1,32-diylbis(oxy))bis(2-(hexadecyloxy)propane-3,1-diyl)bis(2-(trimethylammonio)ethyl) bis(phosphate) (GHGTPC-T32)



First, bromoethyldichlorophosphate was prepared following a reported protocol.⁶⁸ To a solution of bromoethyldichlorophosphate (937 mg, 3.87 mmol) in dry THF (15 mL), a solution of **S5** (510 mg, 0.47 mmol) and Et₃N (0.74 mL, 5.29 mmol) in dry THF (15 mL) was added dropwise. After stirring the mixture for 3 days in the dark at room temperature, toluene (100 mL) was added to precipitate triethylammonium chloride. Then, the solution was filtered through a small pad of celite and the filtrate concentrated. The resulting residue was dissolved in a mixture of THF/NaHCO₃ (sat) (1:1, 100 mL) and the reaction was stirred for 16 hours at room temperature. Solvents were evaporated under vacuum and the resulting aqueous solution was acidified to pH 1 using a dilution solution of HCl (1 mol/L) and extracted using several portions of DCM/MeOH (8:2) (5x30 mL). The organic layers were combined, dried over Na₂SO₄ and concentrated under reduced pressure. The resulting residue was used in the next step without further purification. To a solution of the previous crude intermediate in a mixture of THF/CHCl₃ (2:1) (7.5 mL), Me₃N (33 % in EtOH) (12 mL) was added and the reaction was stirred in a sealed tube at room temperature for 5 days. The reaction mixture was concentrated to dryness, purified on sephadex LH-20 using DCM/MeOH (1:1) as eluent and purified by column chromatography on silica gel using DCM/MeOH/H₂O (70:30:5) as the eluent. Lipid **GHGTPC-T32** (469 mg, 70 %) was obtained as a white gum.

^1H NMR (500 MHz, MeOD- d_4 /CDCl $_3$ - d_1 1:1) δ 4.18 (ddq, $J = 7.3, 5.0, 2.6$ Hz, 4H), 3.83 (t, $J = 5.6$ Hz, 4H), 3.58 – 3.37 (m, 18H), 3.15 (s, 18H), 1.52 – 1.45 (m, 8H), 1.27 – 1.19 (m, 108H), 0.82 (t, $J = 6.9$ Hz, 6H); ^{13}C NMR (126 MHz, MeOD- d_4 /CDCl $_3$ - d_1 1:1) δ 78.0, 78.0, 71.8, 70.7, 70.6, 66.5, 65.1, 58.8, 54.2, 49.3, 49.1, 49.0, 48.8, 48.6, 48.4, 48.2, 31.9, 30.1, 29.7, 29.7, 29.6, 29.4, 26.1, 26.1, 22.7, 14.0; ^{31}P NMR (202 MHz, MeOD- d_4 /CDCl $_3$ - d_1 1:1) δ 0.12. (Figure S6)

4. Sample Preparation

Desired amount of GHGTPC-T32 or DC16:0etherPC were weighted and dissolved in a chloroform / methanol (67:33). The nitrogen is applied to remove the organic solvent and samples were then subjected to the vacuum overnight. The samples were hydrated to 0.1 wt.%, 0.5 wt.%, 1 wt. % and 2.5 wt.% for dynamic light scattering (DLS), differential scanning calorimetry (DSC), SAXS, and NSE measurements. The lipid concentration of GHGTPC-T32 and DC16:0etherPC is further diluted to 0.05 wt.% and 0.003 wt.% for cryo-TEM measurements.

5. Cryogenic Transmission Electron Microscope (cryo-TEM)

The morphology was characterized by an FEI Tecnai G2 F30 twin transmission electron microscope operated at 200 kV. In sample preparation, a 200-mesh lacey carbon grid (Electron Microscopy Sciences) was picked up with tweezers and mounted on the plunging station of an FEI Vitrobot. Four microliters of the solution were applied to the grid in the Vitrobot chamber with 100% humidity. The excess liquid was blotted by filter paper attached to the arms of the Vitrobot for 2 seconds to form a thin liquid film in the grid. Subsequently, the grid was vitrified by plunging into liquid ethane. The vitrified sample was finally transferred onto Gatan's single-tilt cryogenic specimen holder for imaging.

6. Differential Scanning Calorimetry (DSC)

DSC experiments were conducted using a NanoDSC (TA Instruments, New Castle, DE). All the samples were prepared at 0.5 wt.%. ~500 μL of DI water and samples were loaded into the reference and sample cells, respectively. The pressure was kept at 3 atm during the experiments. The data were collected at a rate of 1 $^{\circ}\text{C}/\text{min}$. All the data were also corrected by solvent background after measurements.

7. SAXS Data Analysis

The SAXS experiments were performed on the Life Science X-ray Scattering (LiX) beamline in the National Synchrotron Light Source II (NSLS-II) located at the Brookhaven National Laboratory (BNL, Upton, NY)⁶⁹. The samples were loaded and measured in the fixed cell with two mica windows. SAXS intensity is expressed as a function of the scattering vector, q , ($q \equiv \frac{4\pi}{\lambda} \sin \frac{\theta}{2}$, where θ is the scattering angle) which varies from 0.005 \AA^{-1} to 0.7 \AA^{-1} . The X-ray energy was 13.5 keV. Radial averaging and q -conversion of data were performed using the standard software of merging data from two detectors used in the measurements. Transmission correction and background subtraction were performed to minimize the intensity of the hydrogen bond from water. The SAXS data is analyzed by using SASView 4.2.2.

8. NSE experiments

GHGTPC-T32 and DC_{16:0}etherPC membrane were measured on the NGA NSE spectrometer at the National Institute of Standards and Technology Center for Neutron Research (NCNR).⁷⁰⁻⁷¹ Neutron wavelengths of 8 \AA and 11 \AA with a wavelength spread of $\frac{\Delta\lambda}{\lambda} \approx 20\%$ were used to access a q -range of 0.04 \AA^{-1} to 0.11 \AA^{-1} and Fourier times, t , range from 0.01 ns to 100 ns. The samples with the mass fraction of 2.5 % were contained in a titanium cell with quartz windows at the sample thickness of 1 mm. Temperature was controlled with oil circulation system within the accuracy

better than 1 °C. The measured data were corrected for the instrumental resolution as well as for the background (D₂O solvent) using Data Analysis and Visualization Environment (DAVE).⁷²

9. Dynamic light scattering (DLS)

The instrument is an ALV compact goniometer system with multi-detectors (CGS-3MD, Germany) and the wavelength of He-Ne laser beam is 632.8 nm. The autocorrelation function, $g_1(\tau)$, was collected using ALV-7004 digital multiple tau real time space. The $g_1(\tau)$ can be described as an exponential decay, $e^{-2q^2D\tau}$, where D is the translation diffusion coefficient and q is the scattering vector, $\frac{4n\pi}{\lambda} \sin \frac{\theta}{2}$, with refraction index of solution, n . The scattering angle was set at 90°. Based on the Stokes-Einstein relation and the assumption of spherical shape, the hydrodynamic radius (R_h) is related to D of spherical particles via $R_h = k_B T / 6\pi\eta D$, where k_B and η are the Boltzmann constant and the solvent viscosity, respectively. The plot of R_h distribution was based on intensity-weighted outcomes.

Supporting Information:

DSC thermograms for the GHGTPC-T32 and DC16:0etherPC (Fig S1); DLS outcomes of the GHGTPC-T32 and DC16:0etherPC (Fig S2); The description, scheme and mathematic scattering expression for 5LCSD model (Fig S3); ^1H NMR and ^{13}C NMR of Molecules S4 and S5 (Figs S4 and S5); ^1H NMR, ^{13}C NMR, and ^{31}P NMR of GHGTPC-T32 (Fig S6)

Acknowledgement

The authors would like to acknowledge the beamtime of 16ID-LiX at the NSLS-II (Brookhaven National Lab) through a beamtime proposal (BAG-305637). The LiX beamline is part of the Center for BioMolecular Structure (CBMS), which is primarily supported by the National Institutes of Health, National Institute of General Medical Sciences (NIGMS) through a P30 Grant (P30GM133893), and by the DOE Office of Biological and Environmental Research (KP1605010). LiX also received additional support from NIH Grant S10 OD012331. As part of NSLS-II, a national user facility at Brookhaven National Laboratory, work performed at the CBMS is supported in part by the U.S. Department of Energy, Office of Science, Office of Basic Energy Sciences Program under contract number DE-SC0012704. This work is also benefited from the use of the SasView application, originally developed under NSF Award DMR-0520547. SasView also contains code developed with funding from the EU Horizon 2020 programme under the SINE2020 project Grant No 654000. Access to the NGA-NSE spectrometer was provided by the Center for High Resolution Neutron Scattering, a partnership between the National Institute of Standards and Technology and the National Science Foundation under Agreement No. DMR-2010792. G.L. and J.Y. acknowledge financial support from the Air Force Office of Scientific Research (FA9550-12-1-0435). M.N. acknowledge financial support from National Science Foundation under DMR-1935956.

Certain commercial equipment, instruments, or materials (or suppliers, or software *etc.*) are identified in this paper to foster understanding. Such identification does not imply recommendation

or endorsement by the National Institute of Standards and Technology, nor does it imply that the materials or equipment identified are necessarily the best available for the purpose.

Reference

- 1 Faizi, H. A.; Frey, S. L.; Steinkühler, J.; Dimova, R.; Vlahovska, P. M. Bending rigidity of charged lipid bilayer membranes. *Soft Matter* **2019**, *15*, 6006-6013.
- 2 Kelley, E. G.; Butler, P. D.; Nagao, M. Scaling of lipid membrane rigidity with domain area fraction. *Soft Matter* **2019**, *15*, 2762-2767.
- 3 Lee, C.-H.; Lin, W.-C.; Wang, J. All-optical measurements of the bending rigidity of lipid-vesicle membranes across structural phase transitions. *Phys. Rev. E* **2001**, *64*, 020901.
- 4 Lelkes, P. I. Potential dependent rigidity changes in lipid membrane vesicles. *Biochem. Biophys. Res. Commun.* **1979**, *90*, 656-662.
- 5 Nagao, M.; Kelley, E. G.; Ashkar, R.; Bradbury, R.; Butler, P. D. Probing elastic and viscous properties of phospholipid bilayers using neutron spin echo spectroscopy. *J. Phys. Chem. Lett.* **2017**, *8*, 4679-4684.
- 6 Petrache, H. I., Harries, D. & Parsegian, V. A. in *Macromolecular Symposia*. 39-50 (Wiley Online Library).
- 7 Zemel, A.; Ben-Shaul, A.; May, S. Modulation of the spontaneous curvature and bending rigidity of lipid membranes by interfacially adsorbed amphipathic peptides. *J. Phys. Chem. B* **2008**, *112*, 6988-6996.
- 8 Galimzyanov, T.R.; Molotkovsky, R.J.; Bozdaganyan, M.E.; Cohen, F.S.; Pohl, P.; Akimov, S.A. Elastic membrane deformations govern interleaflet coupling of lipid-ordered domains. *Phys. Rev. Lett.* **2015**, *115*, 088101.
- 9 Fowler, P.; Williamson, J.; Sansom, M.; Olmsted, P. Roles of Interleaflet Coupling and Hydrophobic Mismatch in Lipid Membrane Phase-Separation Kinetics. *J. Am. Chem. Soc.* **2016**, *138*, 11633-11642
- 10 Putzel, G. G.; Uline, M. J.; Szleifer, I.; Schick, M. Interleaflet coupling and domain registry in phase-separated lipid bilayers. *Biophys. J.* **2011**, *100*, 996-1004.
- 11 Capponi, S.; Freitas, J. A.; Tobias, D. J.; White, S. H. Interleaflet mixing and coupling in liquid-disordered phospholipid bilayers. *Biochim. Biophys. Acta, Biomembr.* **2016**, *1858*, 354-362.
- 12 Usuda, H.; Hishida, M.; Kelley, E. G.; Yamamura, Y.; Nagao, M.; Saito, K. Interleaflet coupling of n-alkane incorporated bilayers. *Phys. Chem. Chem. Phys.* **2020**, *22*, 5418-5426.
- 13 Quinn, P. A lipid-phase separation model of low-temperature damage to biological membranes. *Cryobiology* **1985**, *22*, 128-146.
- 14 Heberle, F. A.; Feigenson, G. W. Phase separation in lipid membranes. *Cold Spring Harbor Perspect. Biol.* **2011**, *3*, a004630.
- 15 Hammond, A. T.; Heberle, F. A.; Baumgart, T.; Holowka, D.; Baird, B.; Feigenson, G. W. Crosslinking a lipid raft component triggers liquid ordered-liquid disordered phase separation in model plasma membranes. *Proc. Natl. Acad. Sci.* **2005**, *102*, 6320-6325.
- 16 Galla, H.-J.; Sackmann, E. Chemically induced lipid phase separation in model membranes containing charged lipids: a spin label study. *Biochim. Biophys. Acta, Biomembr.* **1975**, *401*, 509-529.
- 17 Parthasarathy, R.; Yu, C.-h.; Groves, J. T. Curvature-modulated phase separation in lipid bilayer membranes. *Langmuir* **2006**, *22*, 5095-5099.

- 18 Piantavigna, S.; Abdelhamid, M.E.; Zhao, C.; Qu, X.; McCubbin, G.A.; Graham, B.; Spiccia, L.; O'Mullane, A.P.; Martin, L.L. Mechanistic details of the membrane perforation and passive translocation of TAT peptides. *ChemPlusChem* **2015**, *80*, 83-90.
- 19 Riske, K. A.; Amaral, L. Q.; Lamy, M. T. Extensive bilayer perforation coupled with the phase transition region of an anionic phospholipid. *Langmuir* **2009**, *25*, 10083-10091.
- 20 Nieh, M.P.; Raghunathan, V.A.; Pabst, G.; Harroun, T.; Nagashima, K.; Morales, H.; Katsaras, J.; Macdonald, P. Temperature driven annealing of perforations in bicellar model membranes. *Langmuir* **2011**, *27*, 4838-4847.
- 21 Antonov, V. F.; Anosov, A. A.; Norik, V. P.; Smirnova, E. Y. Soft perforation of planar bilayer lipid membranes of dipalmitoylphosphatidylcholine at the temperature of the phase transition from the liquid crystalline to the gel state. *Eur. Biophys. J.* **2005**, *34*, 155-162.
- 22 De Rosa, M.; Gambacorta, A.; Nicolaus, B.; Chappe, B.; Albrecht, P. Isoprenoid ethers; backbone of complex lipids of the archaeobacterium *Sulfolobus solfataricus*. *Biochim. Biophys. Acta, Lipids Lipid Metab.* **1983**, *753*, 249-256.
- 23 Sugai, A.; Uda, I.; Itoh, Y. H.; Itoh, T. The core lipid composition of the 17 strains of hyperthermophilic archaea, Thermococcales. *J. Oleo Sci.* **2004**, *53*, 41-44.
- 24 Gattinger, A.; Günthner, A.; Schloter, M.; Munch, J. Characterisation of Archaea in soils by polar lipid analysis. *Acta Biotechnol.* **2003**, *23*, 21-28.
- 25 Boucher, Y.; Kamekura, M.; Doolittle, W. F. Origins and evolution of isoprenoid lipid biosynthesis in archaea. *Mol. Microbiol.* **2004**, *52*, 515-527.
- 26 Schiller, S. M.; Naumann, R.; Lovejoy, K.; Kunz, H.; Knoll, W. Archaea analogue thiolipids for tethered bilayer lipid membranes on ultrasmooth gold surfaces. *Angew. Chem., Int. Ed.* **2003**, *42*, 208-211.
- 27 Matsuno, Y.; Sugai, A.; Higashibata, H.; Fukuda, W.; Ueda, K.; Uda, I.; Sato, I.; Itoh, T.; Imanaka, T.; Fujiwara, S., Effect of growth temperature and growth phase on the lipid composition of the archaeal membrane from *Thermococcus kodakaraensis*. *Biosci., Biotechnol., Biochem.* **2009**, *73*, 104-108.
- 28 Kim, Y.H.; Leriche, G.; Diraviyam, K.; Koyanagi, T.; Gao, K.; Onofrei, D.; Patterson, J.; Guha, A.; Gianneschi, N.; Holland, G.P.; Gilson, M.K., 2019. Entropic effects enable life at extreme temperatures. *Sci. Adv.* **2019**, *5*, eaaw4783.
- 29 Koyanagi, T.; Leriche, G.; Onofrei, D.; Holland, G.P.; Mayer, M.; Yang, J., Cyclohexane Rings Reduce Membrane Permeability to Small Ions in Archaea-Inspired Tetraether Lipids. *Angew. Chem.* **2016**, *128*, 1922-1925.
- 30 Schroeder, T.B.; Leriche, G.; Koyanagi, T.; Johnson, M.A.; Haengel, K.N.; Eggenberger, O.M.; Wang, C.L.; Kim, Y.H.; Diraviyam, K.; Sept, D.; Yang, J., Effects of lipid tethering in extremophile-inspired membranes on H⁺/OH⁻ flux at room temperature. *Biophys. J.* **2016**, *110*, 2430-2440.
- 31 Komatsu, H.; Chong, P. L.-G. Low permeability of liposomal membranes composed of bipolar tetraether lipids from thermoacidophilic archaeobacterium *Sulfolobus acidocaldarius*. *Biochemistry* **1998**, *37*, 107-115.
- 32 Koyanagi, T.; Leriche, G.; Yep, A.; Onofrei, D.; Holland, G.P.; Mayer, M.; Yang, J., Effect of Headgroups on Small-Ion Permeability across Archaea-Inspired Tetraether Lipid Membranes. *Chem. - Eur. J.*, **2016**, *22*, 8074-8077.

- 33 Leriche, G.; Cifelli, J.L.; Sibucão, K.C.; Patterson, J.P.; Koyanagi, T.; Gianneschi, N.C.; Yang, J., Characterization of drug encapsulation and retention in archaea-inspired tetraether liposomes. *Org. Biomol. Chem.* **2107**, *15*, 2157-2162.
- 34 Lipowsky, R.; Leibler, S. Unbinding transitions of interacting membranes. *Phys. Rev. Lett.* **1986**, *56*, 2541.
- 35 Pozo-Navas, B.; Raghunathan, V.A.; Katsaras, J.; Rappolt, M.; Lohner, K.; Pabst, G., 2003. Discontinuous unbinding of lipid multibilayers. *Phys. Rev. Lett.* **2003**, *91*, 028101.
- 36 Pabst, G.; Katsaras, J.; Raghunathan, V. Enhancement of steric repulsion with temperature in oriented lipid multibilayers. *Phys. Rev. Lett.* **2002**, *88*, 128101.
- 37 Yamada, N.L.; Seto, H.; Takeda, T.; Nagao, M.; Kawabata, Y.; Inoue, K., SAXS, SANS and NSE studies on “unbound state” in DPPC/water/CaCl₂ system. *J. Phys. Soc. Jpn.* **2005**, *74*, 2853-2859.
- 38 Scott, H.L.; Skinkle, A.; Kelley, E.G.; Waxham, M.N.; Levental, I.; Heberle, F.A. On the mechanism of bilayer separation by extrusion, or why your LUVs are not really unilamellar. *Biophys. J.* **2019**, *117*, 1381-1386.
- 39 Mitra et al., *J. Phys. Chem. B* 2016, *120*, 3777–3784; DOI: 10.1021/acs.jpcc.6b02997
- 40 Qian, S.; Sharma, V. K.; Clifton, L. A., Understanding the structure and dynamics of complex biomembrane interactions by neutron scattering techniques. *Langmuir* **2020**, *36*, 15189–15211.
- 41 Nagao, M.; Seto, H., Neutron scattering studies on dynamics of lipid membranes featured *Biophysics Rev.* **2023**, *4*, 021306.
- 42 Sharma, V. K.; Mamontov, E., Multiscale lipid membrane dynamics as revealed by neutron spectroscopy. *Progress in Lipid Research* **2022**, *87*, 101179.
- 43 Ruocco, M.; Makriyannis, A.; Siminovitch, D.; Griffin, R. Deuterium NMR investigation of ether- and ester-linked phosphatidylcholine bilayers. *Biochemistry* **1985**, *24*, 4844-4851.
- 44 Nagle, J. F.; Tristram-Nagle, S. Structure of lipid bilayers. *Biochim. Biophys. Acta, Biomembr* **2000**, *1469*, 159-195.
- 45 Guler, S.D.; Ghosh, D.D.; Pan, J.; Mathai, J.C.; Zeidel, M.L.; Nagle, J.F.; Tristram-Nagle, S., Effects of ether vs. ester linkage on lipid bilayer structure and water permeability. *Chem. Phys. Lipids* **2009**, *160*, 33-44.
- 46 Cheu, C.; Yang, L.; Nieh, M.-P. Refining internal bilayer structure of bicelles resolved by extended-q small angle X-ray scattering. *Chem. Phys. Lipids* **2020**, *231*, 104945.
- 47 Yamauchi, K.; Moriya, A.; Kinoshita, M. Peculiar membrane morphologies of archaeobacterial lipid models: 1, 1'-polymethylenebis (2-alkyl-sn-glycero-3-phosphocholine). *Biochim. Biophys. Acta, Lipids Lipid Metab.* **1989**, *1003*, 151-160.
- 48 Yamauchi, K.; Kinoshita, M. Highly stable lipid membranes from archaeobacterial extremophiles. *Prog. Polym. Sci.* **1993**, *18*, 763-804.
- 49 Leriche, G.; Stengel, D.; Onofrei, D.; Koyanagi, T.; Holland, G.P.; Yang, J. Fusion of Bipolar Tetraether Lipid Membranes Without Enhanced Leakage of Small Molecules. *Sci. Rep.* **2019**, *9*, 1-11.
- 50 Galimzyanov, T. R.; Kuzmin, P. I.; Pohl, P.; Akimov, S. A. Elastic deformations of bolalipid membranes. *Soft matter* **2016**, *12*, 2357-2364.
- 51 Holland, D. P.; Struts, A. V.; Brown, M. F.; Thompson, D. H. Bolalipid membrane structure revealed by solid-state ²H NMR spectroscopy. *J. Am. Chem. Soc* **2008**, *130*, 4584-4585.

- 52 Cuccia, L.A.; Morin, F.; Beck, A.; Hebert, N.; Just, G.; Lennox, R.B.. Spanning or looping? The order and conformation of bipolar phospholipids in lipid membranes using 2H NMR spectroscopy. *Chem. - Eur. J.* **2000**, *6*, 4379-4384.
- 53 Bulacu, M.; Périole, X.; Marrink, S. J. In silico design of robust bolalipid membranes. *Biomacromolecules* **2012**, *13*, 196-205.
- 54 Zilman, A.; Granek, R. Undulations and dynamic structure factor of membranes. *Phys. Rev. Lett.* **1996**, *77*, 4788.
- 55 Zilman, A. G.; Granek, R. Membrane dynamics and structure factor. *Chem. Phys.* **2002**, *284*, 195-204.
- 56 Hoffmann, I.; Michel, R.; Sharp, M.; Holderer, O.; Appavou, M.S.; Polzer, F.; Farago, B.; Gradzielski, M. Softening of phospholipid membranes by the adhesion of silica nanoparticles—as seen by neutron spin-echo (NSE). *Nanoscale* **2014**, *6*, 6945-6952.
- 57 Watson, M. C.; Brown, F. L. Interpreting membrane scattering experiments at the mesoscale: The contribution of dissipation within the bilayer. *Biophys. J.* **2010**, *98*, L9-L11.
- 58 Woodka, A. C.; Butler, P. D.; Porcar, L.; Farago, B.; Nagao, M., Lipid bilayers and membrane dynamics: insight into thickness fluctuations. *Phys. Rev. Lett.* **2012**, *109*, 058102.
- 59 Sharma et al., *Phys.Chem.Chem.Phys.*, 2017, *19*, 2514;
- 60 Sharma et al., *Phys.Chem.Chem.Phys.*, 2019, *21*, 20211; DOI: DOI: 10.1039/c9cp03767e
- 61 Lai, D.; Springstead, J. R.; Monbouquette, H. G. Effect of growth temperature on ether lipid biochemistry in *Archaeoglobus fulgidus*. *Extremophiles* **2008**, *12*, 271-278.
- 62 Sprott, G.; Meloche, M.; Richards, J. Proportions of diether, macrocyclic diether, and tetraether lipids in *Methanococcus jannaschii* grown at different temperatures. *J. Bacteriol.* **1991**, *173*, 3907-3910.
- 63 Boyd, E.; Hamilton, T.; Wang, J.; He, L.; Zhang, C. The role of tetraether lipid composition in the adaptation of thermophilic archaea to acidity. *Front. Microbiol.* **2013**, *4*, 62 .
- 64 Debnath, A.; Mukherjee, B.; Ayappa, K.; Maiti, P. K.; Lin, S.-T. Entropy and dynamics of water in hydration layers of a bilayer. *J. Chem. Phys.* **2010**, *133*, 174704.
- 65 Kučerka, N.; Nieh, M.-P.; Katsaras, J. Fluid phase lipid areas and bilayer thicknesses of commonly used phosphatidylcholines as a function of temperature. *Biochim. Biophys. Acta, Biomembr.* **2011**, *1808*, 2761-2771.
- 66 Febo-Ayala, W.; Morera-Félix, S.L.; Hrycyna, C.A.; Thompson, D.H. Functional Reconstitution of the Integral Membrane Enzyme, Isoprenylcysteine Carboxyl Methyltransferase, in Synthetic Bolalipid Membrane Vesicles, *Biochemistry.* **2006**, *45*, 14683–14694.
- 67 Schroeder, T.B.H.; Leriche, G.; Koyanagi T.; Johnson M.A.; Haengel, K.N.; Eggenberger O.M.; Wang, C.L.; Kim, Y.H.; Diraviyam, K.; Sept, D.; Yang, Y.; Mayer, M. Effects of Lipid Tethering in Extremophile-Inspired Membranes on H⁺/OH⁻ Flux at Room Temperature, *Biophysical Journal.* **2016**, *110*, 2430-2440.
- 68 Bartlett, G.R. Phosphorus assay in column chromatography, *Journal of Biological Chemistry.* **1959**, *234*, 466-468.
- 69 Yang, L.; Antonelli, S.; Chodankar, S.; Byrnes, J.; Lazo, E.; Qian, K., Solution scattering at the Life Science X-ray Scattering (LiX) beamline. *J. Synchrotron Radiat.* **2020**, *27*, 804-812.

- 70 Monkenbusch, M.; Schatzler R.; Richter D. The Jülich neutron spin-echo spectrometer - Design and performance, Nuclear Instruments and Methods in Physics Research Section A: Accelerators, Spectrometers, Detectors and Associated Equipment. **1997**, *339*, 301-323.
- 71 Rosov N.; Rathgeber S.; Monkenbusch, M. Neutron Spin Echo Spectroscopy at the NIST Center for Neutron Research, ACS Symposium Series **1999**, pp. 103-116
- 72 Azuah, T.; Kneller, L.R.; Qiu, Y.; Tregenna-Piggott, P.L.W.; Brown, C.M.; Copley, J.R.D.; Dimeo, R.M. DAVE: A comprehensive software suite for the reduction, visualization, and analysis of low energy neutron spectroscopic data, Journal of Research of the National Institute of Standards and Technology. **2009**, *114*, 341-358.